# IMPROVEMENT TO PERFORMANCE OF SOLID-ROTOR-RINGED LINE-START AXIAL-FLUX PERMANENT-MAGNET MOTOR

## A. Mahmoudi[*], S. Kahourzade, N. A. Rahim, and H. W. Ping

UM Power Energy Dedicated Advanced Centre (UMPEDAC), Engineering Tower, Faculty of Engineering, University of Malaya, Kuala Lumpur, Malaysia

**Abstract**—This paper presents two design-and-analysis cases of a line-start axial-flux permanent-magnet motor: with solid rotor and with composite rotor. For a novel structure of the motor, two concentric unilevel spaced raised rings are added to the inner and outer radii of its rotors to enable auto-start capability. The composite rotor was coated by a thin (0.05 mm) layer of copper. The basic equations for the solid rotor ring were extracted. The motor's lack of symmetry necessitated 3D time-stepping finite element analysis, conducted via Vector Field Opera 14.0, which evaluated the design parameters and predicted the motor's transient performance. Results of the FEA show the composite rotor significantly improving both starting torque and synchronization capability over solid rotor.

## 1. INTRODUCTION

Line-start permanent-magnet (LSPM) motors compete with induction motors in many constant-speed applications such as fans, pumps, and compressors; their fulfilment of electric motor applications is sizeable where high efficiency, small size, high power factor, and high power density are required [1, 2]. They, however, have poor starting torque and poor synchronization (both greatly depending on motor and load parameters), and sometimes they cannot start, or fail to synchronize, post early start-up [3].

Permanent-magnet machines generally can be axial-flux or radial-flux [4]. Advantages of axial-flux permanent-magnet (AFPM)

motors over conventional radial-flux permanent-magnet (RFPM) ones are high torque-to-weight ratio, effectiveness, adjustable air-gap, balanced rotor-stator attractive forces, and better heat-removal [5–8]. Researchers have investigated the effect of start-up and synchronization on performance of line-start radial-flux permanent-magnet (LSRFPM) motors [9–17]. There is no publication yet regarding line-start axial-flux permanent-magnet (LSAFPM) motors.

Solid rotors instead of laminated ones are advantageous in their higher mechanical robustness and lower manufacturing cost. Also, some researchers have shown use of solid rotor in poly-phase induction machine to increase torque per ampere at standstill [18]. Another interesting point about solid-rotor motor is that its effectiveness and power factor can be improved by making it a composite rotor [19–20]. To take advantage of all the above mentioned benefits, an AFPM motor capable of auto-starting is presented here then its specifications are improved. AFPM machine designers have for many years been interested in new configurations, but to the best of our knowledge and from our literature review, work reporting the design of an AFPM motor capable of auto starting has yet to be presented.

AFPM machines can be single-sided or double-sided, with or without armature slots, with or without armature core, with internal or external permanent-magnet rotors, with surface-mounted or interior permanent-magnet, and single-stage or multi-stage [21]. Double-sided configurations have either external stator or external rotor. An external stator means fewer permanent magnets but poor use of winding, whereas an external rotor is considered particularly advantageous to machine topology. Topologies for double-sided AFPM machines are one-stator-two-rotor (TORUS) and two-stator-one-rotor (AFIR) [22]. Slot-less TORUS AFPM configuration is the subject of this paper. Slot-less configuration has lower cogging torque and provides better synchronization. Its end windings are short, so less copper losses. For auto-starting, two concentric unilevel spaced raised rings are added to the inner and the outer radii of the rotor discs that partially covers the stator yoke. The proposed design is novel and has a unique structure. The interaction between the induced eddy-currents in the solid-steel rotor ring and the rotating field in the gap between the ring and the end winding produces electromagnetic torque. In an AFPM motor, radial windings usually produce torque, whereas end windings usually are useless, but in this work end windings, too, produce torque. Unlike traditional radial-flux and axial-flux machines, the proposed LSAFPM motor has a complex magnetic circuit and thus its design requires 3D Finite Element Analysis (FEA).

The paper is organized as follows; Section 2 extracts the basic

equations of the raised rotor-disc rings of the proposed axial-flux motor, Section 3 presents the 3D transient FEA of the designed auto-start solid-rotor-ringed AFPM motor, Section 4 presents and compares the simulation results of electromagnetic field analysis via FEA on the proposed motor topologies (solid rotor and composite rotor), and Section 5 concludes the results.

## 2. FUNDAMENTAL DESIGN CONSIDERATION OF THE RAISED ROTOR-DISC RINGS

Presented are the design details of the raisedrings of the rotor disc for an axial-flux induction motor to obtain the appropriate solid-rotor-ringed axial-flux motor construction. Note that the dimensioning was from the electromagnetic point of view only and that the mechanical constraints were not considered. Fig. 1 is a three-view cross-section of the proposed LSAFPM motor. Figs. 1(a) and (b) are respectively the radial and the axial views. The analytical design of the rotor ringconsidered only the radial component of the flux density because this flux component most influences the motor's starting capability.

Tangential tension $\sigma_{\tan}$ estimates the rotor ring size for the desired torque production. As an alternative to air-gap tangential tension, the magnitude of the internal power $P$ from the rotor volume of the induction machine defines the machine constant $C$ [23]:

$$C = \frac{\pi^2}{\sqrt{2}} k_{W1} A B_{gr\_\max} \tag{1}$$

where $A$ is the linear current density, $B_{gr\_\max}$ the air-gap maximum flux density, and $k_{W1}$ the winding factor of the fundamental harmonic. The machine constant is written as a function of tangential tension [23]:

$$C = \frac{\pi^2}{\sqrt{2}} \sigma_{\tan} \pi^2 k_{W1} \tag{2}$$

From Equations (1) and (2), the tangential tension is:

$$\sigma_{\tan} = \frac{A B_{gr\_\max}}{2} \tag{3}$$

The tangential tension in the air-gap can be calculated from:

$$\sigma_{\tan} = \frac{\tau}{R_{\mathrm{ave}} S_r} \tag{4}$$

where $R_{\mathrm{ave}}$ is the mean value of the rotor ring's inner and outer radii, $S_r$ the rotor ring's surface facing the air-gap between rotor ring and stator surface, and $\tau$ the torque. The tangential force $F_{\tan}$ is:

$$F_{\tan} = \sigma_{\tan} S_r \tag{5}$$

The radial air-gap length $g_r$ between the rotor ring and the stator yoke surface should be selected with especial care. Increment to the air-gap length increases losses of the stator copper and decreases losses of the rotor's eddy current. Minimum loss occurs between the rising copper losses and the rotor's diminishing harmonic eddy current. The highest possible air-gap flux density ensures the attainment of a high-performance maximum-torque solid-rotor-ringed LSAFPM motor.

For acceptable calculation results of the analytical design, the rotor ring and stator were divided into a number of parallel active circular sub-volumes (see Fig. 1(c)). By this, the curve of the machine is assumed to have no effect anymore on the performance of an individual sub-machine. Densities of the rotor and stator flux were studied in each area from $1$ to $n$. Upon selection of the rotor ring slot $b_r$ and stator pitch $\tau_r(1\ldots n)$ widths, the motor's inner parts must not be allowed to saturate. The flux density of the rotor ring tooth is
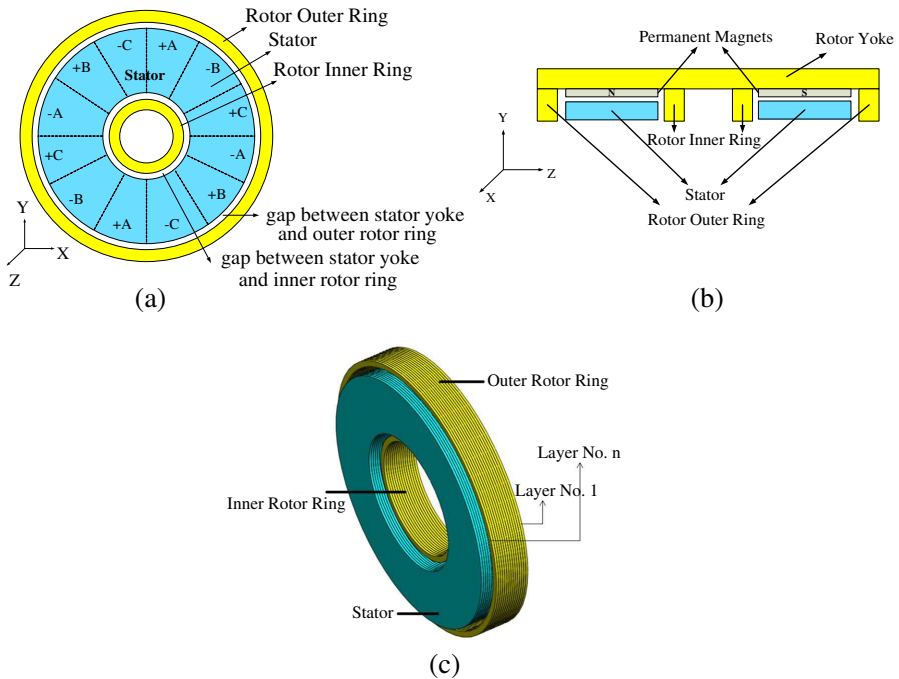


**Figure 1.** 2D and 3D views of the proposed designed motor. Various parts of the motor including stator, rotor disc, rotor ring, air-gap, and winding configurations are illustrated. (a) Radial view. (b) Axial view. (c) Division of the rotor ring into parallel active regions, showing the diameters of the inner and the outer rotor ring.

calculated from:

$$B_{dr(1...n)} = \frac{B_{gr\_\max}\tau_{r(1...n)}}{\tau_{r(1...n)} - b_r} \tag{6}$$

The allowable rotor ring tooth flux density $B_{dr}$ of radial-flux induction machines is between $1.5\,\mathrm{T}$ and $2.2\,\mathrm{T}$ [24] (this range is also used here). Assuming the total flux of the slot pitch to flow along the teeth, no flux in either the slots or their insulation, and non-saturation of the motor teeth, allows calculation of the rotor-ringteeth length:

$$w_{dr} = \frac{\tau_{r(n)}B_{gr\_\max}}{B_{dr(n)}} \tag{7}$$

Thickness of the rotor ring was calculated from:

$$w_{th\_r} = \frac{\phi_{rr}}{2B_{rr}k_{rFe}l_e} \tag{8}$$

where $B_{rr}$ is the flux density peak of the rotor ring, $k_{rFe}$ the rotor iron space coefficient (which depends on the relative thickness of the electric sheet insulation to the press fit of the stack), and $\phi_{rr}$ the peak value for the main radial flux penetrating the stator and the rotor ring. The rotor yoke flux density allowable for radial-flux induction motor is $0.4\,\mathrm{T}$ to $1.6\,\mathrm{T}$ [24] (this range is also used here). The mechanical strength of the solid rotor ring (unlike that of the laminated rotors) was not a problem, where the mechanical constraints may thus determine the minimum thickness of the rotor ring.

The length of the coil depends on the stator core length $l_{ea}$, pole pitch $\tau_p$, chord factor $\chi$ (the ratio of the coil span $W$ to the pole pitch $\tau_p$), and the stator core thickness $l_{er}$:

$$l_m = p\left(2l_{ea} + \chi\tau_{p\_out} + 2l_{er}\right) \tag{9}$$

The end-winding leakage flux results from all the currents flowing into the end windings. The end windings here are the radial windings producing the torque in synchronous state. The geometry of the windings in axial-flux machines is difficult to analyse and all the phases of poly-phase machines influence leakage flux; empirical determination of the inductance factors $\lambda_E$ and $\lambda_W$ is thus sufficient. Richter detailed calculated values of the inductance factors valid for induction machines [25]. The end-winding leakage inductances $L_{WS}$ in the inner ($L_{WS\_\mathrm{in}}$) and the outer ($L_{WS\_\mathrm{out}}$) circumferences of the proposed axial-flux induction machine are:

$$L_{WS\_\mathrm{in}} = \frac{4m}{Q}q \cdot N^2 \cdot \pi \cdot f \cdot \mu_0\left(2 \cdot l_{er} \cdot \lambda_E + \chi \cdot \tau_{p\_in} \cdot \lambda_W\right) \tag{10a}$$

$$L_{WS\_\mathrm{out}} = \frac{4m}{Q}q \cdot N^2 \cdot \pi \cdot f \cdot \mu_0\left(2 \cdot l_{er} \cdot \lambda_E + \chi \cdot \tau_{p\_out} \cdot \lambda_W\right) \tag{10b}$$

where $f$ is the frequency, $Q$ the number of slots, $q$ the number of slots per pole and per phase, and $\mu_0$ the permeability of free space.

## 3. TRANSIENT FINITE ELEMENT ANALYSIS

The motor's design includes an inside-out double-rotor single-stator LSAFPM (see Fig. 2 for an exploded view). The stator has a three-phase winding fixed by housing, each rotor has 4 trapezoidal NdFeB magnets mounted on the rotor disc, and both rotors are supported by holders connected to a bearing-mounted shaft. The motor's auto-start capability comes from two concentric unilevel spaced raised rings added to the inner and the outer radii of the rotors. The structure of the solid rotor and the composite rotor is the same, only the composite rotor is coated by a thin (0.05 mm) copper layer. Table 1 lists the motor's dimensions and specifications.

The governing equations for the FEA are [26]:

$$\nabla \times B = \mu J \tag{11}$$

$$\oint B \cdot dl = \mu \int J \cdot ds \tag{12}$$

$$\nabla \times J = -\sigma \frac{dB}{dt} \tag{13}$$
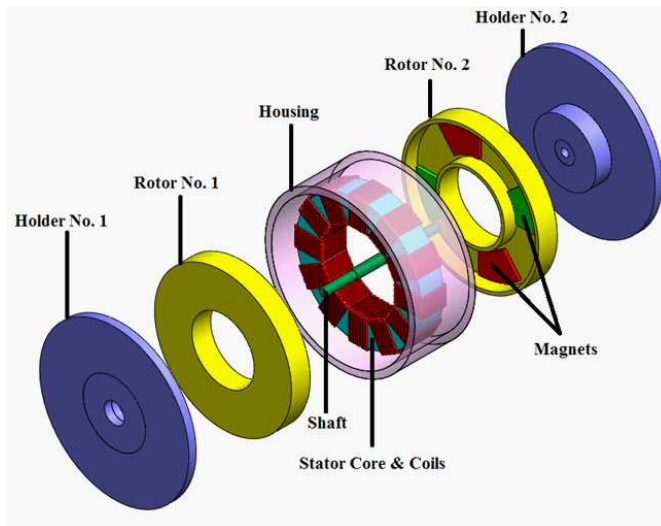
$$B = \nabla \times \psi \tag{14}$$



**Figure 2.** Exploded diagram of the designed motor.

**Table 1.** The motor's dimensions and specifications.

| | | |
|---|---|---|
| Nominal Voltage (*Line-Line* RMS) | $V_{\mathrm{nom}}$ | 220 V |
| Nominal Power | $P_{\mathrm{nom}}$ | 746 W |
| Nominal Torque | $\tau_{\mathrm{nom}}$ | 5.5 Nm |
| Number of Pole Pairs | $p$ | 2 |
| Number of Phases | $m$ | *3* |
| Drive Frequency | $f$ | 50 |
| Stator Outer Diameter | $D_{\mathrm{so}}$ | 230 mm |
| Stator Inner Diameter | $D_{\mathrm{si}}$ | 130 mm |
| Rotor Outer Diameter | $D_{\mathrm{ro}}$ | 240 mm |
| Rotor Inner Diameter | $D_{\mathrm{ri}}$ | 120 mm |
| Ratio of Inner Diameter to Outer Diameter of Stator | $\lambda$ | 0.56 |
| Rotor Ring Axial Length | $L_r$ | 10 mm |
| Magnet's Axial Length | $L_{\mathrm{pm}}$ | 4 mm |
| Pole Pitch | $\gamma_p$ | 100° |
| Stator-Yoke Thickness | $L_{\mathrm{cs}}$ | 38 |
| Rotor-Yoke Thickness | $L_{\mathrm{cr}}$ | 15 mm |
| Number of Winding Turns per Phase | $N_{\mathrm{ph}}$ | 450 |
| Air-Gap Flux Density | $B_g$ | 3.5 |
| Axial Air-Gap Length | $g_a$ | 1 mm |

where $B$, $J$, and $\psi$ respectively are magnetic flux density, current density, and magnetic vector potential. $\sigma$ and $\mu$ are electrical conductivity and magnetic permeability. Considering $H$ as the magnetic field intensity, the preceding equations lead to the following equation:

$$\nabla \times \left( \frac{1}{\sigma} \nabla \times H \right) + \frac{\partial B}{\partial t} = 0 \qquad (15)$$

The result is a formula where vector fields are represented by first-order edge elements and scalar fields by second-order nodal unknowns. Field equations are coupled with the circuit equations for conductors, because in transient simulations, supply voltages are applied and currents are unknown. Classical Newton-Raphson algorithm was used for the nonlinearities. A major difficulty for transient simulation is that induced currents on the rotor rings must be calculated in each step before the torque is calculated.

Note that finite element method (FEM) facilitates field analysis of electromagnetic problems with complex geometries [27–33]. The proposed LSAFPM machine has a unique construction, and its lack
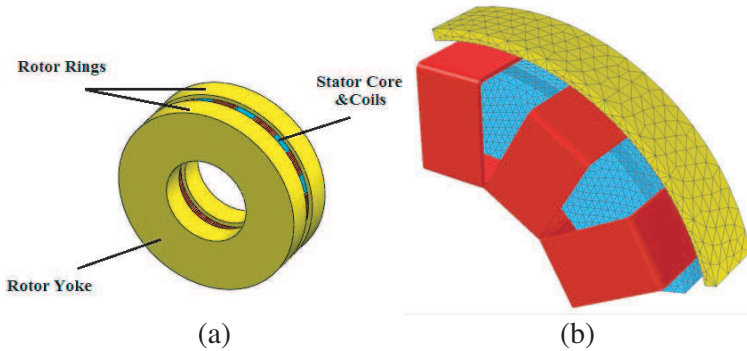
**Figure 3.** Proposed line-start axial-flux permanent-magnet motor. (a) Complete model: The motor structure from the inner to the outer diameter of LSAFPM motor. (b) One eight of the motor: 3D auto-mesh: tetrahedral elements generated on Vector Field Opera 14.0 software.

of symmetry makes 3D-FEA a design requisite. The model's complex magnetic circuit was analysed by 3D-FEA, for an overall view of the saturation levels in various parts of the motor, and to extract the motor's characteristics. An advantage of 3D-FEA is that various components of flux density can be calculated with high accuracy. The design was simulated on commercial Vector Field Opera 14.0 3D software [34]. Corresponding materials and circuit currents were assigned to each model block. The motor's symmetric 3D model was divided into eight parts, making each a one-magnetic-pole piece. Only one of the eight was used, so simulation/calculation time was shortened.

Figure 3(a) shows the whole machine comprising 12 coils and 2 pole-pairs. Fig. 3(b) shows only one eighth of the motor modelling the structure of the FEA-designed LSAFPM, 90 degrees of the entire motor structure and 1 pole, fulfilling symmetry conditions. Fig. 3(b) (generated on Vector Field Opera 14.0 software) is a 3D auto-mesh: tetrahedral elements with 6 nodes fitting circular shape of the layers starting from the inner to the outer diameter of the LSAFPM motor [34].

Figure 4 depicts the magnetic flux density distribution in various sectors of the LSAFPM motor. Evaluation of the magnetic flux density is important because the flux density saturation of the stator or the rotor affects the motor operation and reduces the efficiency. Fig. 4 shows the magnetic flux density distribution in both solid-rotor and composite-rotor LSAFPM motors post synchronization, when the
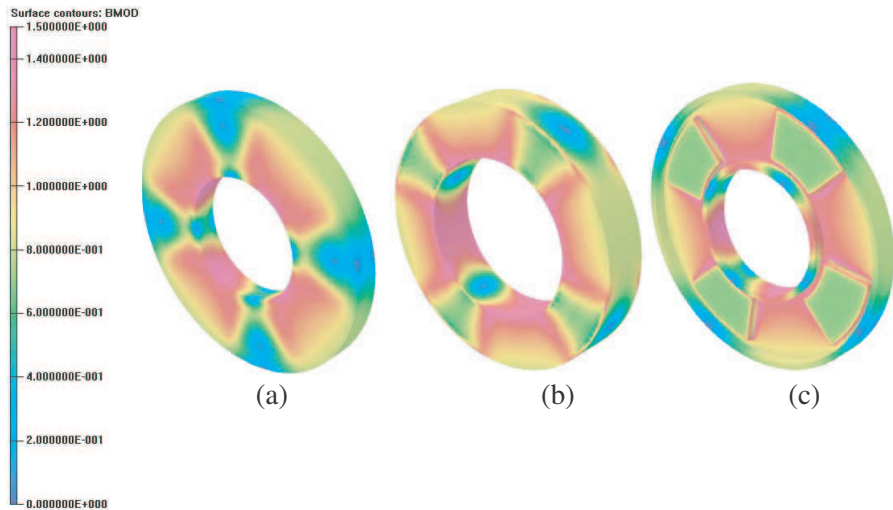
**Figure 4.** Field analysis of the LSAFPM motor, in vector field opera 14.0. (a) 1st rotor: Flux-density plot in first rotor. (b) stator: Flux density plot in stator. (c) 2nd rotor: Flux density plot in second rotor.

copper layer has almost no influence on the motor's behaviour. The magnetic flux density distribution for both the solid and the composite rotors are thus the same.

The only difference between the solid and the composite rotors is the thin copper layer deposited on the solid-iron rotor; all other parameters equal. Fig. 5 is the air-gap flux-density distribution, in average radius and under full-load and no-load conditions. The maximum flux density is $0.7\,\mathrm{T}$, averaging $0.35\,\mathrm{T}$. Fig. 6 shows induced no-load back EMF at synchronous speed (1500). The harmonics appearing in back EMF waveform is due to the usage of the trapezoidal permanent magnets without consideration of any optimization technique.

## 4. COMPARING THE SOLID WITH THE COMPOSITE

The LSAFPM motor starts as an induction motor by the resultant of two torque components: cage torque and opposing magnet torque (braking torque). When the motor speed approaches synchronous speed, synchronization begins and the motor operates in synchronous state (no eddy current except harmonic field current flows into the solid rotor bars then). In that state, two torque components (the reluctance and the synchronous) mobilize the rotor. [35] describes the dynamic
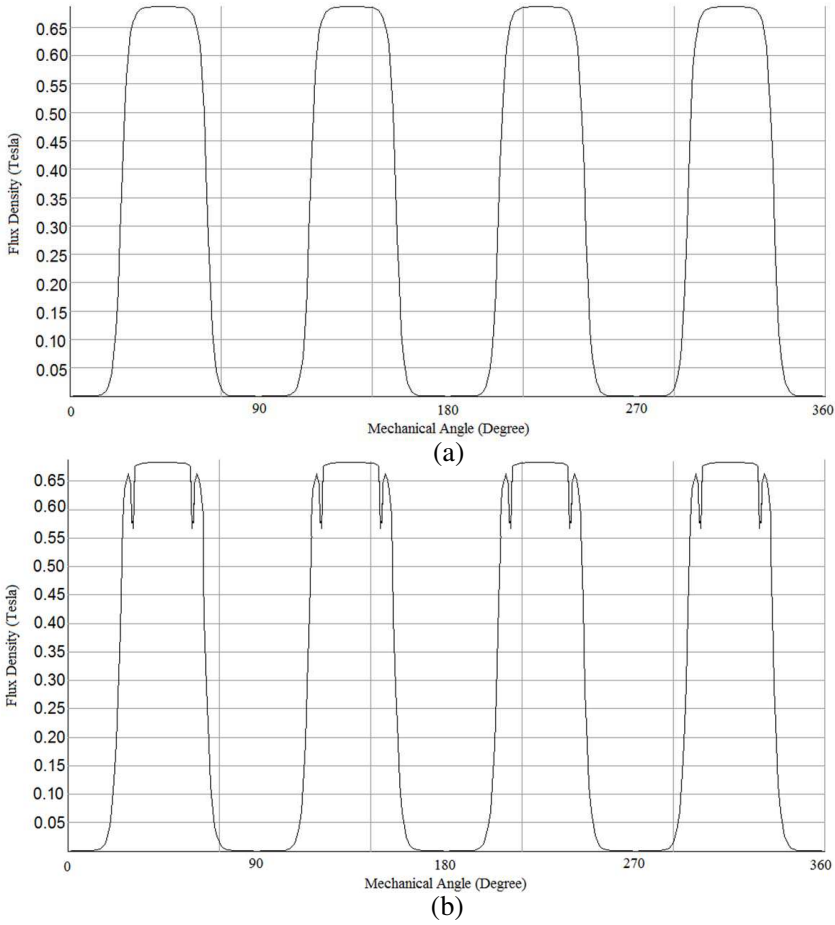
**Figure 5.** Distribution of air-gap magnetic flux density, for the average radius. (a) No load. (b) Full load.

performance of line-start permanent-magnet motors in a stationary $d$-$q$ reference frame:

$$V_{sq} = r_s i_{sq} + \omega_r \lambda_{sd} + \frac{d\lambda_{sq}}{dt} \tag{16}$$

$$V_{sd} = r_s i_{sd} - \omega_r \lambda_{sq} + \frac{d\lambda_{sd}}{dt} \tag{17}$$

$$V'_{rq} = r'_{rq} i'_{rq} + \frac{d\lambda'_{rq}}{dt} = 0 \tag{18}$$

$$V'_{rd} = r'_{rd} i'_{rd} + \frac{d\lambda'_{rd}}{dt} = 0 \tag{19}$$

where $V_{sq}$, $V_{sd}$, $V'_{rq}$, and $V'_{rd}$ are the stator voltages and the rotor voltages, $\lambda_{sq}$, $\lambda_{sd}$, $\lambda'_{rq}$, and $\lambda'_{rd}$ the stator linkage fluxes and the rotor linkage fluxes, and $i_{sq}$, $i_{sd}$, $i'_{sq}$, and $i'_{sd}$ the stator currents and the rotor currents, $\omega_r$, $r_s$, $r'_{rd}$, and $r'_{rq}$ respectively the rotor speed, stator resistance, and rotor resistances (all relative to the stator). The stator linkage flux and the rotor linkage flux are:

$$\lambda_{sq} = L_{sq}i_{sq} + L_{mq}i'_{rq} \tag{20}$$

$$\lambda_{sd} = L_{sd}i_{sd} + L_{md}i'_{rd} + \lambda'_m \tag{21}$$

$$\lambda'_{rq} = L'_{rq}i'_{rq} + L_{mq}i_{sq} \tag{22}$$

$$\lambda'_{rd} = L'_{rd}i'_{rd} + L_{md}i_{sd} + \lambda'_m \tag{23}$$

where $L_{sq}$, $L_{sd}$, $L'_{rq}$, $L'_{rd}$ are the stator self-inductances and the rotor self-inductances, $L_{mq}$ and $L_{md}$ the mutual inductances, and $\lambda'_m$ the permanent-magnet flux. The electromagnetic torque is then [35]:

$$T_{em} = \frac{3p}{2}(L_{sd} - L_{sq})i_{sd}i_{sq} + \frac{3p}{2}(L_{md}i'_{rd}i_{sq} - L_{mq}i'_{rq}i_{sd}) + \frac{3p}{2}\lambda'_m i_{sq} \tag{24}$$

with the first term being the reluctance torque, the second term the cage torque, and the third term the magnet's synchronous torque. The motor dynamic is:

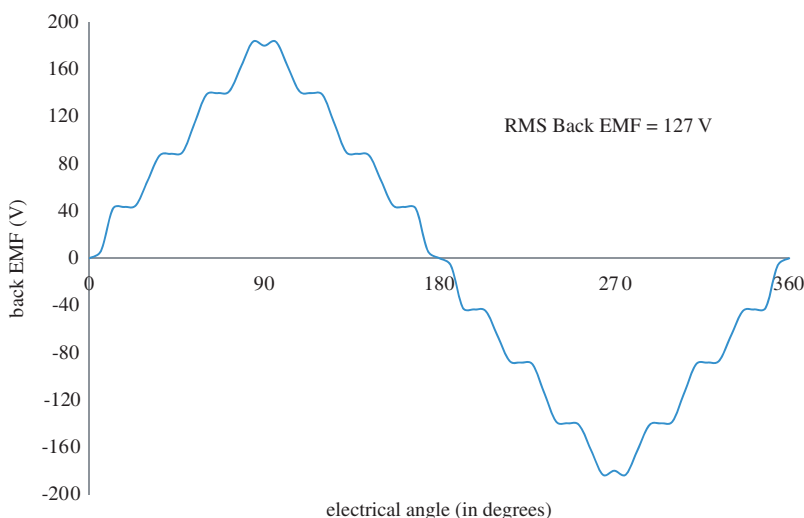$$T_{em} - T_l - C_v\omega_r = j\frac{d\omega_r}{dt} \tag{25}$$



**Figure 6.** Back EMF at synchronous speed (1500 rpm).

with $j$, $C_v$, and $T_l$ respectively being the moment of inertia, the viscosity coefficient, and the load torque. Fig. 7 gives a schematic view of the $d$-$q$ equivalent circuits of the proposed LSAFPM motor.

Line start synchronous motor is a low-cost solution that works reasonably well if the motor load and power supply voltage remain mostly constant. The performance comparison of the solid versus the composite treated the proposed LSAFPM motors as an induction motor, without any permanent magnets, simulated by FEA. The stator was excited via a three-phase voltage supply; the motors then began rotating as induction motors and at sub-synchronous speeds. They draw high current at start-up, so star-delta starter was used to start the proposed synchronous motors as induction motors. The composite rotor was shown to produce more induced torque at any given slip. Fig. 8 gives the motors' induced-torque curves. At any slip, the motor with the composite rotor produced the higher torque than did the motor with the solid rotor.

The starting and the synchronizing of LSAFPM motors are feats. The challenge factor is the braking torque of the magnet poles. Fig. 9
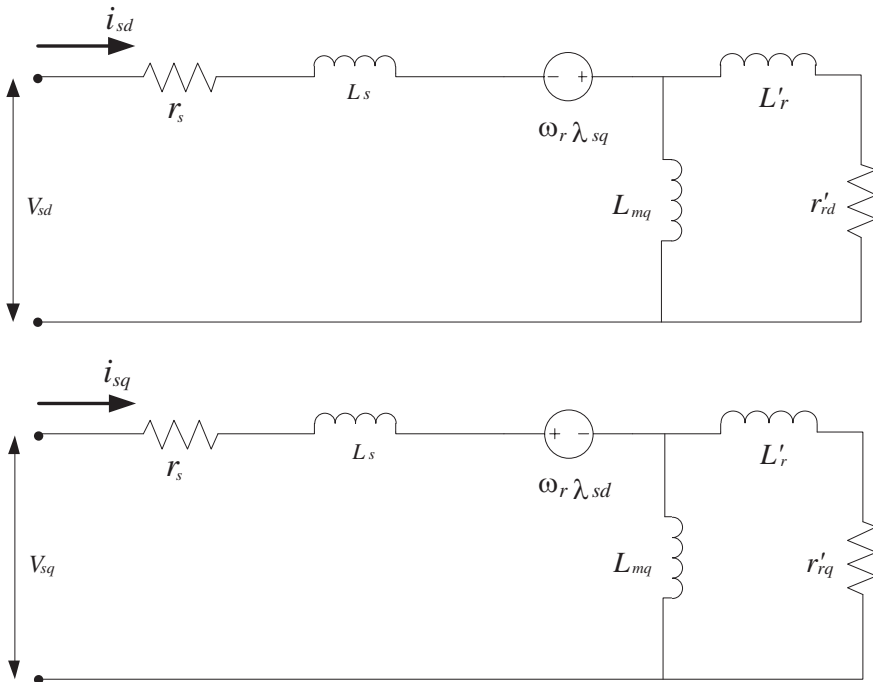


**Figure 7.** A $d$-$q$ reference frame equivalent circuit of proposed LSAFPM motor.
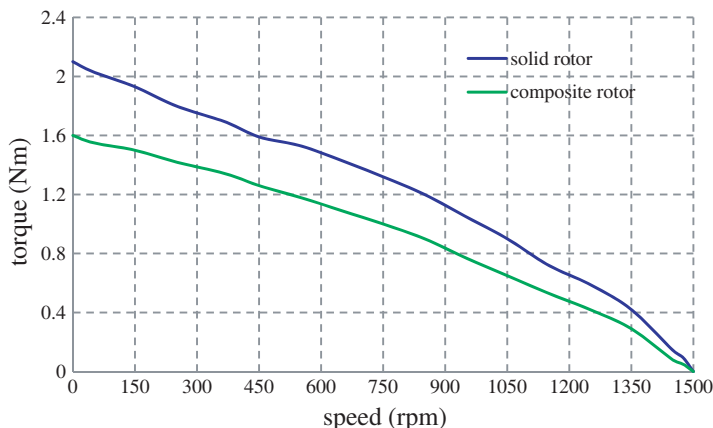
**Figure 8.** Induced induction torque of both solid and composite rotors.
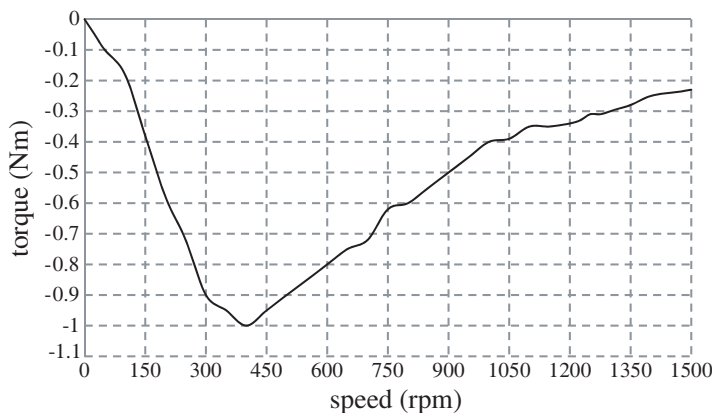


**Figure 9.** Braking torque caused by permanent magnets during start up.

shows the permanent-magnet braking torque calculated via FEA for the LSAFPM motor. This torque is developed between starting and synchronous speed. It reaches the maximum at low speed (see Fig. 9). The braking torque is [36]:

$$T_b = \frac{3pr_s(1-s)E_0^2}{2\omega_s} \times \frac{r_s^2 + X_{sq}^2(1-s)^2}{(r_s^2 + X_{sd}X_{sq}(1-s)^2)} \quad (26)$$

with $E_0$, $X_{sd}$, $X_{sq}$, $\omega_s$, and $s$ respectively being the magnet back-EMF, the $d$-axis stator reactance, the $q$-axis stator reactance, the synchronous angular frequency, and the slip. This torque resists the

cage torque and may cause failures in starting or synchronizing.

The simulation results show that with similar loads, the composite rotor had faster start-up and shorter settling time. Figs. 10 and 11 show the transient response of the solid-rotor LSAFPM and the composite-rotor LSAFPM to various loads. Interaction between the
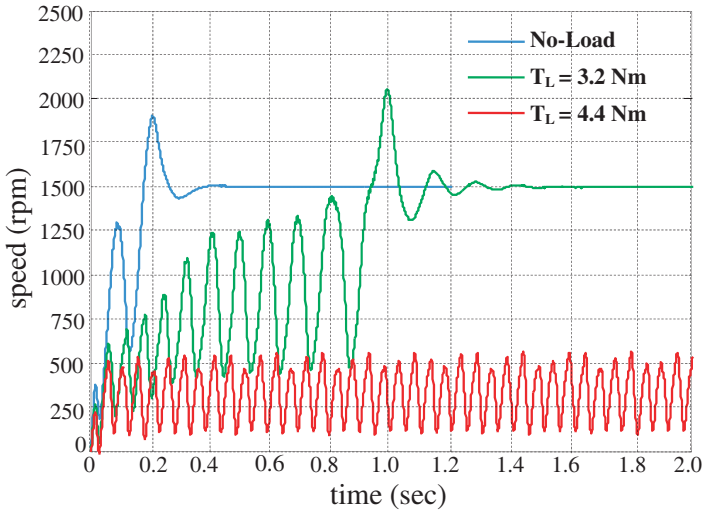


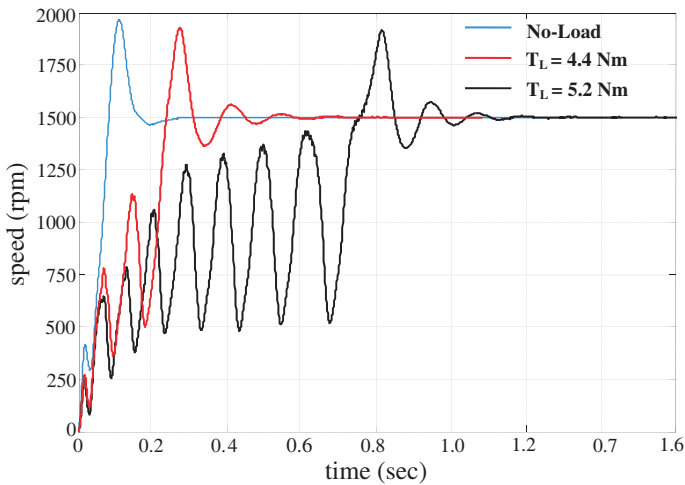**Figure 10.** Simulation results of the solid-rotor LSAFPM motor under various load torques.



**Figure 11.** Simulation results of the composite-rotor LSAFPM under various load torques.
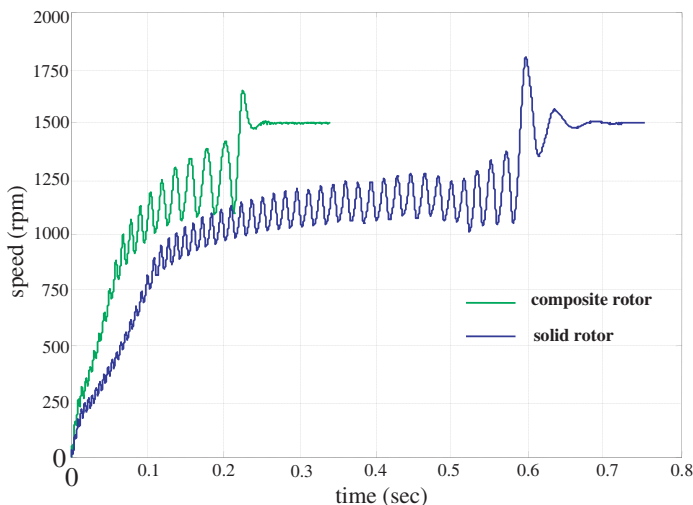
**Figure 12.** Simulation results of the LSAFPMs under $j_L = 5j_r$.

eddy-currents in the solid-steel rotor ring and the rotating field in the air-gap between the ring and the end winding produces electromagnetic torque. The eddy currents affect the motors' performance. The thin copper layer on the rotor-ring surface increases material conductivity, increasing current to the rotor-ring surface during start-up. The composite rotor maintains the mechanical advantages of the solid rotor but improves the rotor's electrical characteristics through low rotor resistance at low slip; the torque induced at any given slip of the composite-rotor LSAFPM motor thus increases. The composite rotor outperforms the solid rotor through faster start-up and shorter settling time.

The other interesting result is the maximum load torque at which the motors can drive. As Fig. 10 shows, with 4.4 Nm load torque, the solid rotor failed to synchronize and started to oscillate between 100 rpm and 550 rpm whereas the composite rotor could drive the given load successfully. The load torque was then increased to 5.2 Nm for the composite rotor; the motor could synchronize with the load but failed to drive higher levels of load torque (see Fig. 11).

Another simulation verified the results for which the inertia of the load $(j_L)$ was five times as much as the inertia of the rotor $(j_r)$. Inline-start motors the inertia of the load matters to synchronization. The higher the inertia, the worse the synchronization. The simulation results show the solid rotor just able to synchronize the load torque of $j_L = 5j_r$ after $t = 24$ s, whereas the composite rotor took only $t = 0.7$ s; see Fig. 12.

## 5. CONCLUSIONS

This paper presented the design and the finite element analysis of two types of LSAFPM motor. A typical solid-rotor LSAFPM motor was designed and simulated by 3D-FEA method. Results of the simulation show this type of motor to have some deficiencies. The starting torque is low and a long time is needed to synchronize. To overcome these deficiencies, a copper-coated rotor is proposed. A thin layer of copper is deposited on the outer face of the solid rotors. 3D transient FEA results show considerable improvement to the starting torque and the synchronization. The thin layer of copper on the rotor-ring surface increased conductivity of the material and caused more current to circulate on the rotor-ring surface during start-up. The torque induced at any given slip of the composite-rotor LSAFPM motor thus increased. In conclusion, composite-rotor LSAFPM motor is advantageous over solid-rotor LSAFPM motor in the former's capability to improve synchronization and drive heavier loads. These advantages of the composite rotor lead to the idea for its application in low-cost LSAFPM motors.

## APPENDIX A. NOMENCLATURE

| | |
|---|---|
| $A$ | linear current density |
| $B$ | magnetic flux density |
| $B_{dr}$ | rotor ring tooth flux density |
| $B_{gr\_max}$ | air-gap maximum flux density |
| $B_{rr}$ | peak flux density of rotor ring |
| $C$ | machine constant |
| $C_v$ | viscosity coefficient |
| $D_{so}$ | stator outer diameter |
| $D_{si}$ | stator inner diameter |

| | |
|---|---|
| $D_{ro}$ | rotor outer diameter |
| $D_{ri}$ | rotor inner diameter |
| $E_0$ | magnet back-EMF |
| $F_{\tan}$ | tangential force |
| $H$ | magnetic field intensity |
| $J$ | current density |
| $L_{cr}$ | rotor-yoke thickness |
| $L_{cs}$ | stator-yoke thickness |
| $L_{sd}$ | d-axis component of stator self-inductance |
| $L_{sq}$ | q-axis component of stator self-inductance |
| $L'_{rd}$ | d-axis component of rotor self-inductance |
| $L'_{rq}$ | q-axis component of rotor self-inductance |
| $L_{md}$ | d-axis component of stator mutual-inductance |
| $L_{mq}$ | q-axis component of stator mutual-inductance |
| $L_{pm}$ | magnet's axial length |
| $L_r$ | rotor ring axial length |
| $L_W$ | end winding leakage inductances |
| $L_{SW\_in}$ | end winding leakage inductances at inner radius |
| $L_{SW\_out}$ | end winding leakage inductances at outer radius |
| $N_{ph}$ | number of winding turns per phase |
| $P$ | power |
| $P_{nom}$ | nominal power |
| $Q$ | number of slots |
| $R_{ave}$ | average inner and outer radii of rotor ring |
| $S_r$ | rotor ring's surface facing the air-gap between rotor ring and stator surface |
| $T_{em}$ | electromagnetic torque |
| $T_l$ | load torque |
| $T_b$ | breaking torque |
| $V_{sd}$ | d-axis component of stator voltage |
| $V_{sq}$ | q-axis component of stator voltage |
| $V'_{rd}$ | d-axis component of rotor voltage referred to stator |
| $V'_{rq}$ | q-axis component of rotor voltage referred to stator |
| $V_{nom}$ | nominal voltage |
| $W$ | coil span |

| | |
|---|---|
| $W_{dr}$ | length of rotor-ring teeth |
| $W_{th\_r}$ | depth of rotor-ring teeth |
| $X_{sd}$ | d-axis component of stator reactance |
| $X_{sq}$ | q-axis component of stator reactance |
| $b_r$ | rotor ring slot width |
| $f$ | frequency |
| $g_a$ | axial air-gap length |
| $g_r$ | radial air-gap length |
| $i_{sd}$ | d-axis component of stator current |
| $i_{sq}$ | q-axis component of stator current |
| $i'_{rd}$ | d-axis component of rotor current referred to stator |
| $i'_{rq}$ | q-axis component of rotor current referred to stator |
| $j$ | moment of inertia |
| $j_L$ | load inertia |
| $j_r$ | rotor inertia |
| $k_{W1}$ | winding factor of fundamental harmonic |
| $k_{rFe}$ | space factor of the iron |
| $l_{ea}$ | equivalent stator core length |
| $l_{er}$ | equivalent stator core thickness |
| $l_m$ | length of one turn of the winding |
| $m$ | number of phases |
| $n$ | number of concentric circular divisions for rotor ring and stator |
| $p$ | number of pole pairs |
| $q$ | number of slots per pole per phase |
| $r'_{rd}$ | d-axis component of rotor resistances referred to stator |
| $r'_{rq}$ | q-axis component of rotor resistances referred to stator |
| $r_s$ | stator resistance |
| $s$ | slip |
| $\gamma_p$ | pole pitch |
| $\lambda$ | ratio of inner diameter to outer diameter of stator |
| $\lambda_{sd}$ | d-axis component of stator flux linkage |
| $\lambda_{sq}$ | q-axis component of stator flux linkage |
| $\lambda'_{rd}$ | d-axis component of rotor flux linkage |
| $\lambda'_{rq}$ | q-axis component of rotor flux linkage |

$\lambda'_m$       *permanent magnet flux*
$\lambda_E$       *empirical inductance factor*
$\lambda_W$       *empirical inductance factor*
$\mu$       *magnetic permeability*
$\mu_0$       *Permeability of free space*
$\mu_r$       *Relative permeability*
$\sigma$       *electrical conductivity*
$\sigma_{\tan}$       *tangential tension*
$\tau$       *torque*
$\tau_{nom}$       *nominal torque*
$\tau_p$       *pole pitch*
$\tau_{p\_in}$       *pole pitch at inner radius*
$\tau_{p\_out}$       *pole pitch at outer radius*
$\tau_r$       *rotor ring slot pitch*
$\psi$       *magnetic vector potential*
$\varphi_{rr}$       *peak value for the main radial flux penetrating the rotor ring*
$\chi$       *chord factor*
$\omega_r$       *rotor speed*
$\omega_s$       *synchronous speed*

## REFERENCES

1. Fei, W., P. Luk, J. Ma, J. X. Shen, and G. Yang, "A high-performance line-start permanent magnet synchronous motor amended from a small industrial three-phase induction motor," *IEEE Transactions on Magnetics*, Vol. 45, No. 10, 4724–4727, Oct. 2009.

2. Knight, A. M. and C. I. McClay, "The design of high-efficiency line-start motors," *IEEE Transactions on Industry Applications*, Vol. 36, No. 36, 1555–1562, Nov.–Dec. 2000.

3. Aliabad, A. D., M. Mirsalim, and N. F. Ershad, "Line-start permanent-magnet motors: significant improvements in starting torque, synchronization, and steady-state performance," *IEEE Transactions on Magnetics*, Vol. 46, No. 12, 4066–4072, Dec. 2010.

4. Cavagnino, A., M. Lazzari, F. Profumo, and A. Tenconi, "A comparison between the axial flux and the radial flux structures for PM synchronous motors," *IEEE Transaction on Industrial Applications*, Vol. 38, No. 6, 1517–1524, Nov.–Dec. 2002.

5.  Mahmoudi, A., N. A. Rahim, and W. P. Hew, "Analytical method for determining axial-flux permanent-magnet machine sensitivity to design variables," *International Review of Electrical Engineering (IREE)*, Vol. 5, No. 5, 2039–2048, Sep.–Oct. 2010.

6.  Mahmoudi, A., N. A. Rahim, and W. P. Hew, "An analytical complementary fea tool for optimizing of axial-flux permanent-magnet machines," *International Journal of Applied Electromagnetics Machines (IJEAM)*, Vol. 37, No. 1, 19–34, Sept. 2011.

7.  Mahmoudi, A., N. A. Rahim, and H. W. Ping, "Genetic algorithm and finite element analysis for optimum design of slotted torus axial-flux permanent-magnet brushless DC motor," *Progress In Electromagnetics Research B*, Vol. 33, 383–407, 2011.

8.  Rahim, N. A., W. P. Hew, and A. Mahmoudi, "Axial-flux permanent-magnet brushless DC traction motor for direct drive of electric vehicle," *International Review of Electrical Engineering (IREE)*, Vol. 6, No. 2, 760–769, Apr. 2011.

9.  Ding, T., N. Takorabet, F. M. Sargos, and X. Wang, "Design and analysis of different line-start pm synchronous motors for oil-pump applications," *IEEE Transactions on Magnetics*, Vol. 45, No. 3, 1816–1819, Mar. 2009.

10. Honsinger, V. B., "Permanent magnet machines: Asychronous operation," *IEEE Transactions on Power Apparatus and Systems*, Vol. 99, No. 4, 1503–1509, Jul. 1980.

11. Kim, B. T. and B. I. Kwon, "Influence of space harmonics on starting performance of a single-phase line start permanent-magnet motor," *IEEE Transactions on Magnetics*, Vol. 44, No. 22, 4668–4672, Dec. 2008.

12. Marcic, T., B. Stumberger, G. Stumberger, M. Hadziselimovic, P. Virtic, and D. Dolinar, "Line-starting three-and single-phase interior permanent magnet synchronous motors — direct comparison to induction motors," *IEEE Transactions on Magnetics*, Vol. 44, No. 11, 4413–4416, Nov. 2008.

13. Miller, T. J. E., "Synchronization of line-start permanent-magnet AC motors," *IEEE Transactions on Power Apparatus and Systems*, Vol. 103, No. 7, 1822–1828, Jul. 1984.

14. Peralta-Sánchez, E. and A. Smith, "Line-start permanent-magnet machines using a canned rotor," *IEEE Transactions on Industry Applications*, Vol. 45, No. 3, 903–910, May-Jun. 2009.

15. Rahman, M. A. and T. A. Little, "Dynamic performance analysis of permanent magnet synchronous motors magnet synchronous motors," *IEEE Transactions on Power Apparatus and Systems*, Vol. 103, No. 6, 1277–1282, Jun. 1984.

16. Rahman, M. A., A. M. Osheiba, and M. A. Choudhury, "Run-up response of polyphase permanent magnet synchronous motors," *Electric Machines and Power Systems*, Vol. 9, No. 4–5, 347–356, 1984.

17. Rahman, M. A., A. M. Osheiba, and T. S. Radwan, "Synchronization process of line-start permanent magnet synchronous motors," *Electric Machine and Power Systems*, Vol. 25, No. 6, 577–592, 1997.

18. Sarma, M., "Current-density distribution in solid-rotor induction motor," *IEEE Transactions on Magnetics*, Vol. 15, No. 6, 1473–1475, Nov. 1979.

19. Sarma, M. S. and G. R. Soni, "Solid-rotor and composite-rotor induction machines," *IEEE Transactions on Aerospace and Electronic Systems*, Vol. 8, No. 2, 147–155, Mar. 1972.

20. Wilson, J. C., E. A. Erdelyi, and R. E. Hopkins, "Aerospace composite-rotor induction motors," *IEEE Transactions on Aerospace*, Vol. 3, No. 2, 18–23, Jun. 1965.

21. Mahmoudi, A., N. A. Rahim, and W. P. Hew, "Axial-flux permanent-magnet machine modeling, design, simulation, and analysis," *Scientific Research and Essay (SRE)*, Vol. 6, No. 12, 2525–2549, Jun. 2011.

22. Mahmoudi, A., N. A. Rahim, and W. P. Hew, "TORUS and AFIR axial-flux permanent-magnet machines: A comparison via finite Element Analysis," *International Review on Modelling and Simulations (IREMOS)*, Vol. 4, No. 2, 624–631, Apr. 2011.

23. Müller, G., K. Vogt, and B. Ponick, *Berechnung Elektrischer Maschinen*, Wiley-VCH, Weinheim, 2008.

24. Vogt, K. and G. Muller, *Elektrische Maschinen Berechnung Rotierender Elektrischer Maschinen*, VebVerlagTechnik, Berlin, 1988.

25. Richter, R. and R. Brüderlink, *ElektrischeMaschinen: Die Induktionsmaschinen*, Vol. 4, BirkhäuserVerlag, Basel, 1954.

26. Bianchi, N., *Electrical Machine Analysis using Finite Element*, Taylor & Francis, CRC Press, 2005.

27. Mahmoudi, A., N. A. Rahim, and W. P. Hew, "Axial-flux permanent-magnet motor design for electric vehicle direct drive using sizing equation and finite element analysis," *Progress In Electromagnetics Research*, Vol. 122, 467–496, 2012.

28. Zhao, W., M. Cheng, R. Cao, and J. Ji, "Experimental comparison of remedial single-channel operations for redundant flux-switching permanent-magnet motor drive," *Progress In Electromagnetics*

*Research*, Vol. 123, 189–204, 2012.

29. Jian, L., G. Xu, G. Yu, J. Song, J. Liang, and M. Chang, "Electro-magnetic design and analysis of a novel magnetic-gear-integrated wind power generator using time-stepping finite element method," *Progress In Electromagnetics Research*, Vol. 113, 351–367, 2011.

30. Touati, S., R. Ibtiouen, O. Touhami, and A. Djerdir, "Experimental investigation and optimization of permanent magnet motor based on coupling boundary element method with permeances network," *Progress In Electromagnetics Research*, Vol. 111, 71–90, 2011.

31. Torkaman, H. and E. Afjei, "FEM analysis of angular misalignment fault in srm magnetostatic characteristics," *Progress In Electromagnetics Research*, Vol. 104, 31–48, 2010.

32. Torkaman, H. and E. Afjei, "Comparison of two types of dual layer generator in field assisted mode utilizing 3D-FEM and experimental verification," *Progress In Electromagnetics Research B*, Vol. 23, 293–309, 2010.

33. Vaseghi, B., N. Takorabet, and F. Meibody-Tabar, "Transient finite element analysis of induction machines with stator winding turn fault," *Progress In Electromagnetics Research*, Vol. 95, 1–18, 2009.

34. Opera Version 14.0 User Guide, Vector Fields, 2011, http://www.cobham.com.

35. Ong, C. M., *Dynamic Simulation of Electric Machinery: Using MATLAB/Simulink*, Prentice Hall PTR, New Jersey, 1998.

36. HassanpourIsfahani, A. and S. Vaez-Zadeh, "Line start permanent magnet synchronous motors: Challenges and opportunities," *Energy*, Vol. 34, No. 11, 1755–1763, Nov. 2009.